Comparison of Two SVPWM Control Strategies of Five-Phase Fault-Tolerant Permanent-Magnet Motor

Guohai Liu, *Senior Member, IEEE*, Li Qu, Wenxiang Zhao, *Senior Member, IEEE*, Qian Chen, and Ying Xie

***Abstract*—Five-phase fault-tolerant permanent-magnet motors incorporate the merits of high-efficiency and high fault-tolerant capability. By adopting the fault-tolerant control technique, these motors can continue operating even fault occurs. This paper proposes two space vector pulse-width modulation (SVPWM) control strategies, namely the symmetric one and the asymmetric one. The novelty of the proposed SVPWM control strategies includes two parts. One is that voltage vector locations in both SVPWM strategies are reconfigured based on a new vector space diagram. Another is that the process of switching vector calculation under fault is similar to that under healthy condition. A five-phase fault-tolerant permanent-magnet motor drive is developed and the proposed fault-tolerant control strategies are evaluated in terms of the torque, voltage, current waveforms, and total harmonic distortion. Simulated and experimental results are provided to verify the effectiveness of the theoretical analysis.**

***Index Terms*—Fault-tolerant control, five-phase motor, space vector pulse-width modulation (SVPWM), torque.**

I. Introduction

MULTIPHASE variable-speed motor drives have received increasing attention [1]–[3]. Since the multiphase motor can still work under fault condition, they are suitable for high-reliability applications, such as aerospace, electric vehicle, and ship propulsion [4]–[6].

In order to improve voltage capability and reduce harmonic distortion, space vector pulse-width modulation (SVPWM) technique has been successfully applied to multiphase drive systems [7]–[13]. The multilevel multiphase SVPWM algorithm was carried out for two- and five-level five-phase induction motors in [7] and [8]. In [9], multiphase SVPWM was used for a seven-phase drive system. Dujic *et al*. in [10] and [11] compared two space vector methods for a five-phase induction motor drive. However, only health condition is considered in the existing SVPWM techniques, rather than fault-tolerant operation. When the motor operates under fault condition, the system parameter variation will deteriorate the operating performance of the energy conversion.

Manuscript received January 30, 2015; revised June 2, 2015 and September 22, 2015; accepted October 28, 2015. Date of publication November 10, 2015; date of current version March 25, 2016. This work was supported in part by the National Natural Science Foundation of China (61273154 and 51422702), by the Natural Science Foundation of Jiangsu Province (BK20130011), and by the Priority Academic Program Development of Jiangsu Higher Education Institutions. Recommended for publication by Associate Editor F. Khan. *(Corresponding author: Wenxiang Zhao)*

The authors are with the School of Electrical and Information Engineering, Jiangsu University, Zhenjiang 212013, China (e-mail: ghliu@ujs.edu.cn; 1007965597@qq.com; zwx@ujs.edu.cn; chenqian0501@163.com; xieying 1234520@126.com).

Color versions of one or more of the figures in this paper are available online at http://ieeexplore.ieee.org.

Digital Object Identifier 10.1109/TPEL.2015.2499211

On the other hand, many fault-tolerant control strategies have been proposed for multiphase motors. The postfault performances of a five-phase fault-tolerant permanent-magnet (PM) motor were evaluated in [14]. When the motor operates under one-phase or two-phase fault, the average torque reduces and the torque ripple increases [14]–[17]. Then, the basic rules of fault-tolerant current control strategies for other five-phase PM motors were proposed. In [18], a model-based predictive control was introduced to manage pre and postfault operations for a five-phase induction motor drive. In [19], a new approach based on mirror symmetry of healthy phase current with respect to the single-phase open-circuit fault location was proposed. Generally, hysteresis current PWM is adopted to realize these fault-tolerant control strategies [20]–[22], even in a vector-control fault-tolerant flux-switching motor drive [23]. However, high switching frequency will increase switching losses of inverter. In [24], an intelligent complementary sliding-mode control was proposed for a six-phase PM motor. This motor was divided into two three-phase motors and each of them was modulated by conventional SVPWM. When one phase of any three-phase motor is open, this three-phase motor will be disconnected and the whole system becomes a three-phase PM motor drive. A control strategy of multiphase induction motors with an odd number of phases under open-circuit phase faults was proposed in [25]. The harmonic currents were used to compensate the main order current produced by healthy SVPWM control strategy. Then, the finally combined currents were realized by carrier-based PWM rather than SVPWM, though carrier-based PWM is so much like SVPWM [26].

In this paper, two SVPWM strategies will be proposed for a five-phase PM motor with open-circuit fault. In the first strategy, the sequence selection under fault condition is similar to that under healthy condition, which is termed as the symmetric SVPWM strategy because of symmetric switching vector in every sector. While the switching vector of another strategy in every sector is asymmetric, the second strategy is called as asymmetric SVPWM control. Although voltage vector locations in both SVPWM strategies are reconfigured based on a new vector space diagram, the process of switching vector calculation under fault is similar to that under healthy condition. Then, the proposed strategies are simple and easily realized. The analyzed modulation strategies will be introduced and presented in Section II. The restructured coordinate system and specific space-vector selections will also be addressed. Then, in Sections III and IV, the comparisons in terms of torque, current, and its harmonic between two schemes will be discussed, and both simulation and experimental results will be presented to verify the effectiveness of the proposed strategies. Finally, the conclusions will be summarized in the last section.

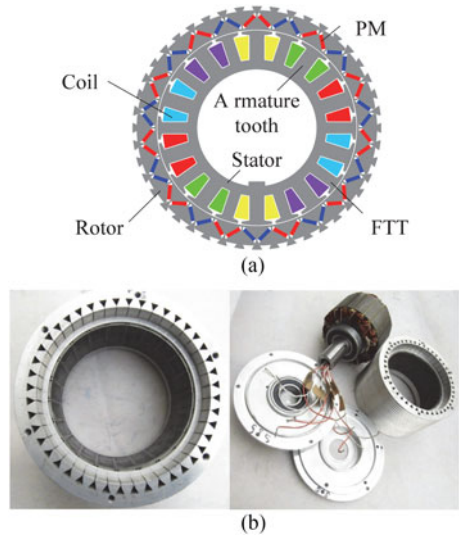

Fig. 1. Five-phase fault-tolerant PM motor. (a) Cross section. (b) Prototype.

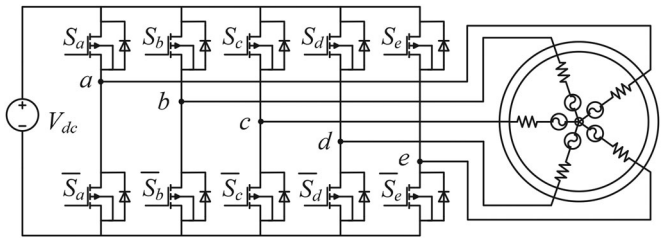

Fig. 2. Drive topology of five-phase fault-tolerant PM motor.

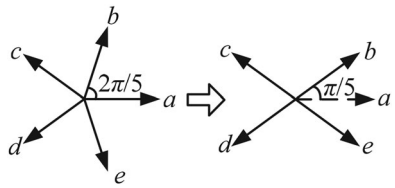

Fig. 3. Pre and postfault vector space diagrams.

II. Proposed PWM Techniques

A five-phase fault-tolerant PM motor with fractional-slot concentrated-windings is shown in Fig. 1. Its rated power is 2 kW, the amplitude of PM flux-linkage is 0.041 Wb, the pole-pair number is 11, the stator resistance is 1 Ω, and the inductance is 1.7 mH [27]. It adopts outer-rotor topology to achieve prominent dynamic performance of the electric vehicle which can enhance torque capability. Moreover, since it adopts single-layer concentrated-windings and fault-tolerant tooth, this motor inherently possesses fault-tolerant characteristic. Furthermore, due to its V-shape PMs and eccentric armature tooth, this motor can provide sinusoidal back- electromotive force, which results in smooth torque and low torque ripple. In addition, it has relatively large *d*-axis inductance, thus offering wide speed range.

Fig. 2 is the drive topology of the five-phase PM motor. $S_a - S_e$ are the switches and $V_{\rm dc}$ is the dc line voltage. The space phases of the five-phase currents in healthy condition are shown in Fig. 3. The stator phases magnetic motive forces (MMFs) are as follows:

$$\begin{cases} \mathrm{MMF}_a = \frac{N}{2} I\cos\varphi\cos(\omega t) \\ \mathrm{MMF}_b = \frac{N}{2} I\cos\left(\varphi - \frac{2\pi}{5}\right)\cos\left(\omega t - \frac{2\pi}{5}\right) \\ \mathrm{MMF}_c = \frac{N}{2} I\cos\left(\varphi - \frac{4\pi}{5}\right)\cos\left(\omega t - \frac{4\pi}{5}\right) \\ \mathrm{MMF}_d = \frac{N}{2} I\cos\left(\varphi + \frac{4\pi}{5}\right)\cos\left(\omega t + \frac{4\pi}{5}\right) \\ \mathrm{MMF}_e = \frac{N}{2} I\cos\left(\varphi + \frac{2\pi}{5}\right)\cos\left(\omega t + \frac{2\pi}{5}\right) \end{cases} \quad (1)$$

where N is the total number of turns for each phase, I is the amplitude of phase current, and φ is the spatial angle.

The stator total MMF can be derived as the sum of MMFs of all the phases:

$$\begin{aligned} \mathrm{MMF}_t = {} & \mathrm{MMF}_a(\varphi,\omega t) + \mathrm{MMF}_b(\varphi,\omega t) + \mathrm{MMF}_c(\varphi,\omega t) \\ & + \mathrm{MMF}_d(\varphi,\omega t) + \mathrm{MMF}_e(\varphi,\omega t) \end{aligned} \quad (2)$$

which is given as

$$\mathrm{MMF}_t(\varphi,\omega t) = \frac{5}{4}(NI\cos(\omega t - \varphi)) \quad (3)$$

Then, (3) can be rewritten as

$$\mathrm{MMF}_t(\varphi,\omega t) = \frac{5}{8} NI(e^{j\omega t}e^{-j\varphi} + e^{-j\omega t}e^{j\varphi}). \quad (4)$$

The total MMF can be also described as

$$\begin{aligned} \mathrm{MMF}_t = {} & \frac{1}{4}\{N[(i_a + e^{-j\frac{2\pi}{5}} i_b + e^{-j\frac{4\pi}{5}} i_c + e^{j\frac{4\pi}{5}} i_d \\ & + e^{j\frac{2\pi}{5}} i_e)e^{j\varphi} + (i_a + e^{j\frac{2\pi}{5}} i_b + e^{j\frac{4\pi}{5}} i_c \\ & + e^{-j\frac{4\pi}{5}} i_d + e^{-j\frac{2\pi}{5}} i_e)e^{-j\varphi}]\}. \end{aligned} \quad (5)$$

Based on (4) and (5), it can be obtained

$$\frac{5}{2} Ie^{j\omega t} = i_a + e^{j\frac{2\pi}{5}} i_b + e^{j\frac{4\pi}{5}} i_c + e^{-j\frac{4\pi}{5}} i_d + e^{-j\frac{2\pi}{5}} i_e. \quad (6)$$

When phase A is open, i_a will be zero. For the purpose of keeping the MMF unchanged, the amplitudes and phases of should be adjusted. Since (6) have multiple sets of solutions, the principle of amplitude equal is selected in this study. Assume the currents after fault have the following relationship:

$$\begin{cases} i'_b = -i'_d \\ i'_c = -i'_e \end{cases}. \quad (7)$$

The remaining currents are found to be

$$\begin{cases} i'_a = 0 \\ i'_b = 1.382I\cos(\omega t - \frac{\pi}{5}) \\ i'_c = 1.382I\cos(\omega t - \frac{4\pi}{5}) \\ i'_d = 1.382I\cos(\omega t + \frac{4\pi}{5}) \\ i'_e = 1.382I\cos(\omega t + \frac{\pi}{5}) \end{cases}. \quad (8)$$

Then, the vector space diagram under open-fault condition will change as shown in Fig. 3. It can be observed that phase B and phase E shift $\pi/5$, while phase C and phase D remain original place. Because of this new diagram, the magnitude and direction of the space vectors also change.

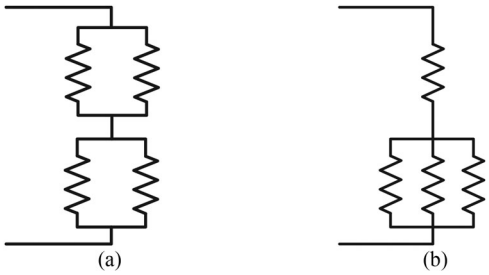

Fig. 4. Basic equivalent circuit configurations. (a) C22. (b) C13.

TABLE I
VALUES OF SWITCHING VECTORS

Vectors	S_b, S_c, S_d, S_e	Magnitude
V_0	0000	0
V_1	0001	0.4 $U_{\rm dc}$
V_2	0010	0.4 $U_{\rm dc}$
V_3	0011	0.4702 $U_{\rm dc}$
V_4	0100	0.4 $U_{\rm dc}$
V_5	0101	0
V_6	0110	0.6472 $U_{\rm dc}$
V_7	0111	0.4 $U_{\rm dc}$
V_8	1000	0.4 $U_{\rm dc}$
V_9	1001	0.6472 $U_{\rm dc}$
V_{10}	1010	0
V_{11}	1011	0.4 $U_{\rm dc}$
V_{12}	1100	0.4702 $U_{\rm dc}$
V_{13}	1101	0.4 $U_{\rm dc}$
V_{14}	1110	0.4 $U_{\rm dc}$
V_{15}	1111	0

Since S_a and $\overline{S}_a$ are abandoned, the five-phase inverter becomes a four-phase one. Since "1" stands for opened switch and "0" is on behalf of closed switch, there are $2^4 = 16$ different switching states. In the four-phase inverter, there are two types of basic equivalent circuit configurations, namely $\{\text{C22}\}$ and $\{\text{C13}\}$, as compared in Fig. 4. Fig. 4(a) is that two upper switches are open and other two lower switches are open, while Fig. 4(b) is that one upper switch is open and three lower switches are open or in an opposite manner. For example, the switching pattern (1100) belongs to $\{\text{C22}\}$, and (1000) belongs to $\{\text{C13}\}$.

The values of these 16 switching vectors can be derived as

$$V_s = \frac{2}{5} V_{\rm dc} \cdot \left(S_b \cdot e^{j\frac{\pi}{5}} + S_c \cdot e^{j\frac{4\pi}{5}} + S_d \cdot e^{-j\frac{4\pi}{5}} + S_e \cdot e^{-j\frac{\pi}{5}} \right) \tag{9}$$

which are listed in Table I. Also, its postfault sector distribution is described in Fig. 5. Since the vectors are decomposed to α-axis and β-axis, the sector is calculated as shown in Fig. 6. However, since V_5 and V_{10} belong to $\{\text{C22}\}$, the currents from phase B to phase E are not zero. It conflicts to the calculated results by (9). So, they can be ignored and there are only 14 useful switching vectors.

According to the control requirement, the purpose of postfault PWM strategy is continuing faulty operation with low torque ripple and acceptable current magnitude. Then, two postfault SVPWM strategies will be proposed and discussed.

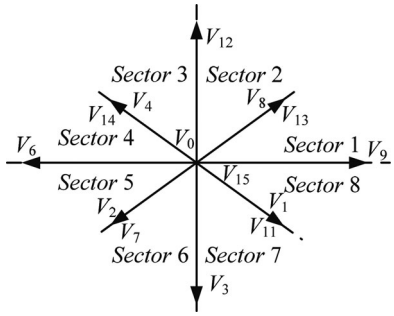

Fig. 5. Postfault voltage vectors in α-β space.

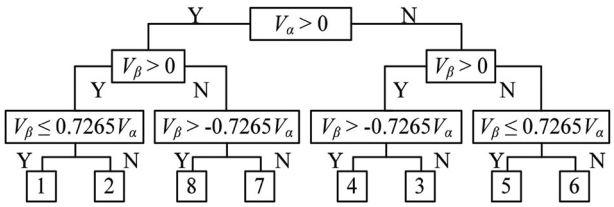

Fig. 6. Sector calculation.

A. Asymmetric PWM signals

The first one of the proposed SVPWM schemes can generate asymmetric PWM signals. Due to different magnitudes, 14 voltage space vectors can be classified as 12 nonvanishing vectors and two vanishing vectors. Each sector selects three nonvanishing vectors and two vanishing vectors to comprise the reference vector. The first and last vectors are V_0 and V_{15}, respectively, which leads to the asymmetry of this scheme. Besides, to minimize the total switching losses, a device switches only once during each period. For example, in sector 1, the sequence of selected space vectors is $V_{15}(1111) \rightarrow V_{13}(1101) \rightarrow V_9(1001) \rightarrow V_8(1000) \rightarrow V_0(0000)$. Fig. 7 shows the switching vectors in all sectors.

Since V_8 and V_{13} have identical magnitude and direction, their actuation durations can be considered the same each other. Assuming that the actuation durations are T_0, T_1, and T_2 as shown in Fig. 8, sine theorem can be used to calculate the duration as

$$\frac{T_1 V_8}{\sin\theta} T_s = \frac{V_{\rm ref}}{\sin(4\pi/5)} = \frac{T_2 V_9}{\sin(\pi/5 - \theta)} T_s \tag{10}$$

where T_s is PWM period.

Based on the relationship between the reference vector and the α–β coordinate system, it can be defined as

$$\begin{cases} V_\alpha = V_{\rm ref}\cos\theta \\ V_\beta = V_{\rm ref}\sin\theta \\ \text{Value1} = V_\alpha \sin(\pi/5) - V_\beta \cos(\pi/5) \\ \text{Value2} = V_\alpha \sin(\pi/5) + V_\beta \cos(\pi/5) \end{cases}. \tag{11}$$

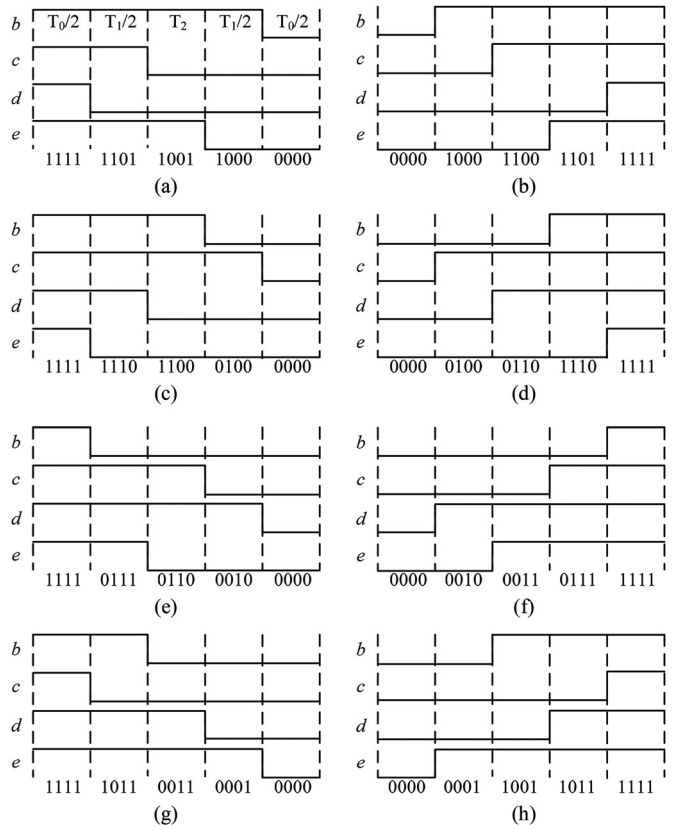

Fig. 7. Switching vectors in all sectors. (a) Sector 1. (b) Sector 2. (c) Sector 3. (d) Sector 4. (e) Sector 5. (f) Sector 6. (g) Sector 7. (h) Sector 8.

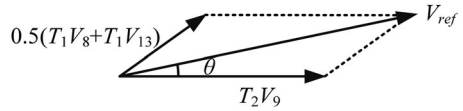

Fig. 8. Actuation duration in sector 1.

After taking the values of V_8 and V_9, and (11) into consideration, the time intervals in sector 1 can be obtained as

$$\begin{cases} T_1 = \frac{V_\beta}{0.4V_{\rm dc}\cdot\sin(\pi/5)}T_s \\ T_2 = \frac{\rm Value1}{0.6472V_{\rm dc}\cdot\sin(\pi/5)}T_s \end{cases}. \tag{12}$$

By using this calculation method, the whole actuation durations in all sectors can be achieved as listed in Table II.

B. Symmetric PWM signals

Since both the initial one and the ending one are the vanishing vectors, the second scheme gives symmetric PWM signals. The first method can be used to define the sectors and calculate the actuation duration. Fig. 9 shows the different identifications of space vectors. In each sector, the lower switches of two phases keep open and the switches of other phases still change once in every period. Compared to the first method, the second SVPWM scheme removes two vectors in one sector as shown in Fig. 10.

TABLE II
ACTUATION DURATIONS IN EACH SECTOR

Sector	T_1	T_2
1	$\frac{V_\beta}{0.4V_{\rm dc}\cdot\sin(\pi/5)}T_s$	$\frac{\rm Value1}{0.6472V_{\rm dc}\cdot\sin(\pi/5)}T_s$
2	$\frac{V_\alpha}{0.4V_{\rm dc}\cdot\sin(3\pi/10)}T_s$	$\frac{-\rm Value1}{0.4702V_{\rm dc}\cdot\sin(3\pi/10)}T_s$
3	$\frac{-V_\alpha}{0.4V_{\rm dc}\cdot\sin(3\pi/10)}T_s$	$\frac{\rm Value2}{0.4702V_{\rm dc}\cdot\sin(3\pi/10)}T_s$
4	$\frac{V_\beta}{0.4V_{\rm dc}\cdot\sin(\pi/5)}T_s$	$\frac{-\rm Value2}{0.6472V_{\rm dc}\cdot\sin(\pi/5)}T_s$
5	$\frac{-V_\beta}{0.4V_{\rm dc}\cdot\sin(\pi/5)}T_s$	$\frac{-\rm Value1}{0.6472V_{\rm dc}\cdot\sin(\pi/5)}T_s$
6	$\frac{-V_\alpha}{0.4V_{\rm dc}\cdot\sin(3\pi/10)}T_s$	$\frac{\rm Value1}{0.4702V_{\rm dc}\cdot\sin(3\pi/10)}T_s$
7	$\frac{V_\alpha}{0.4V_{\rm dc}\cdot\sin(3\pi/10)}T_s$	$\frac{-\rm Value2}{0.4702V_{\rm dc}\cdot\sin(3\pi/10)}T_s$
8	$\frac{-V_\beta}{0.4V_{\rm dc}\cdot\sin(\pi/5)}T_s$	$\frac{\rm Value2}{0.6472V_{\rm dc}\cdot\sin(\pi/5)}T_s$

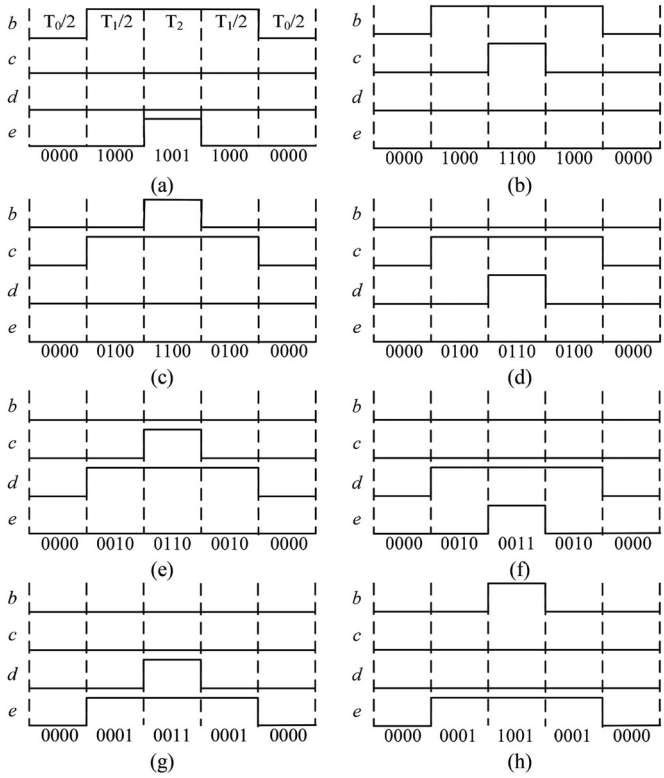

Fig. 9. Switching vectors in each sector. (a) Sector 1. (b) Sector 2. (c) Sector 3. (d) Sector 4. (e) Sector 5. (f) Sector 6. (g) Sector 7. (h) Sector 8.

III. SIMULATION

The five-phase fault-tolerant PM motor drive by using proposed two SVPWM methods will be simulated for verification in this section. The control diagram is shown in Fig. 11. During the simulation, *d*-axis current is set to 0 A and the reference speed is 300 r/min. The SVPWM strategy changes while the operation is from health to faulty conditions. The currents i_d and i_q, and speed are generated to construct a close loop. The rotor

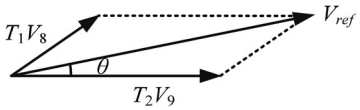

Fig. 10. Actuation duration in sector 1.

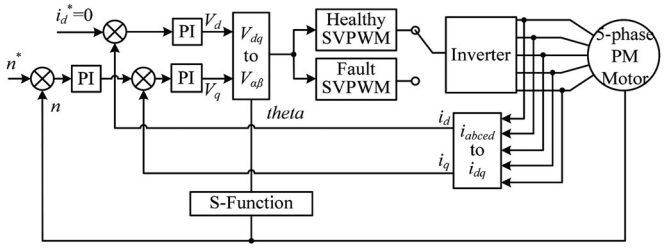

Fig. 11. Control diagram of drive system.

position is derived by using speed *S*-function. The relationship between speed and angle can be described as

$$\begin{cases} \Omega = 2\pi n/60 \\ \omega = np \cdot \Omega \\ d\omega/dt = (T_e - T_L)/J \\ d\theta/dt = \omega \end{cases} \tag{13}$$

where Ω is the mechanical angular speed, ω is the electrical angular speed, n is the response speed, np is the pole-pair number, T_e is the electromagnetic torque, T_L is the load torque, J is the moment of inertia, and θ is the electrical angle of the rotor position.

Regardless of the operation situation, the current transformation matrix is

$$T = \frac{2}{5}\begin{bmatrix} 1 & \cos\left(\frac{2\pi}{5}\right) & \cos\left(\frac{4\pi}{5}\right) & \cos\left(\frac{6\pi}{5}\right) & \cos\left(\frac{8\pi}{5}\right) \\ 0 & \sin\left(\frac{2\pi}{5}\right) & \sin\left(\frac{4\pi}{5}\right) & \sin\left(\frac{6\pi}{5}\right) & \sin\left(\frac{8\pi}{5}\right) \\ 1 & \cos\left(\frac{4\pi}{5}\right) & \cos\left(\frac{8\pi}{5}\right) & \cos\left(\frac{2\pi}{5}\right) & \cos\left(\frac{6\pi}{5}\right) \\ 0 & \sin\left(\frac{4\pi}{5}\right) & \sin\left(\frac{8\pi}{5}\right) & \sin\left(\frac{2\pi}{5}\right) & \sin\left(\frac{6\pi}{5}\right) \\ 1/2 & 1/2 & 1/2 & 1/2 & 1/2 \end{bmatrix}. \tag{14}$$

The dc link voltage is 50 V, and the load is 5 Nm. When the fault occurs at 0.05 s, the phase A current becomes to 0 suddenly. Then, the duty cycle, phase current, and voltage change according to different SVPWM methods. The speed and torque responses are compared in Fig. 12. It can be seen that both methods can track the reference speed regardless of the operation situation. Also, the torque ripple is insignificant. The duty, stator current waveforms, and associated spectra are shown in Figs. 13 and 14. The current total harmonic distortions are obtained by fast Fourier transform analysis.

Since the four phases current are separately symmetrical as shown in Fig. 3, the currents of phase B and phase E are chosen as example. By comparing the five-phase stator current in Figs. 13(b) and 14(b), the asymmetric SVPWM offers an almost

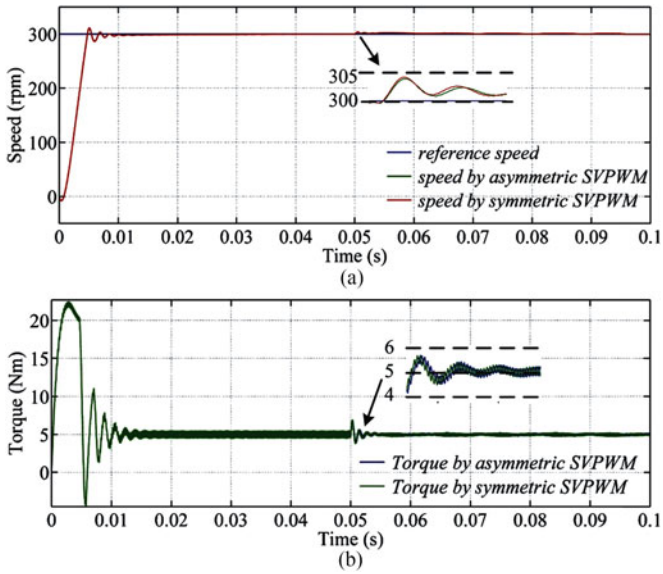

Fig. 12. Speed and torque responses for two SVPWM methods. (a) Speed. (b) Torque.

up–down symmetric current. However, the symmetric SVPWM gives an asymmetric current. After extracting one cycle of the fault operation current, it is obvious that two methods have different harmonics. The asymmetric SVPWM has the third-order harmonic and the symmetric SVPWM has the second-order one. The magnitude of harmonic and the values of current total harmonic distortion have been calculated as shown in Figs. 13 and 14. As shown in Figs. 7 and 9, the switching devices of both SVPWM methods change four times. However, each switching device of the asymmetric SVPWM method changes one time during a period, while the symmetric SVPWM method keeps two switching devices normal close. From the perspective of the duty cycle, for example, in sector 1, the turn-on time of the switching devices by the asymmetric SVPWM method and the symmetric SVPWM method are described as the following, respectively:

$$\begin{cases} \text{duty\_}b = 1 - T_0/2 \\ \text{duty\_}c = (T_1 + T_0)/2 \\ \text{duty\_}d = T_0/2 \\ \text{duty\_}e = T_2 + (T_1 + T_0)/2 \end{cases} \tag{15}$$

$$\begin{cases} \text{duty\_}b = T_1 + T_2 \\ \text{duty\_}c = 0 \\ \text{duty\_}d = 0 \\ \text{duty\_}e = T_2 \end{cases}. \tag{16}$$

Based on the above duty cycle, the asymmetric SVPWM method is continuous, while the symmetric SVPWM method is discontinuous. Since the half of the duty cycle by the symmetric SVPWM method is zero, the high-side switching devices will lead to more currents amplitude than the low-side switching by this method. So, the symmetric SVPWM have rough current.

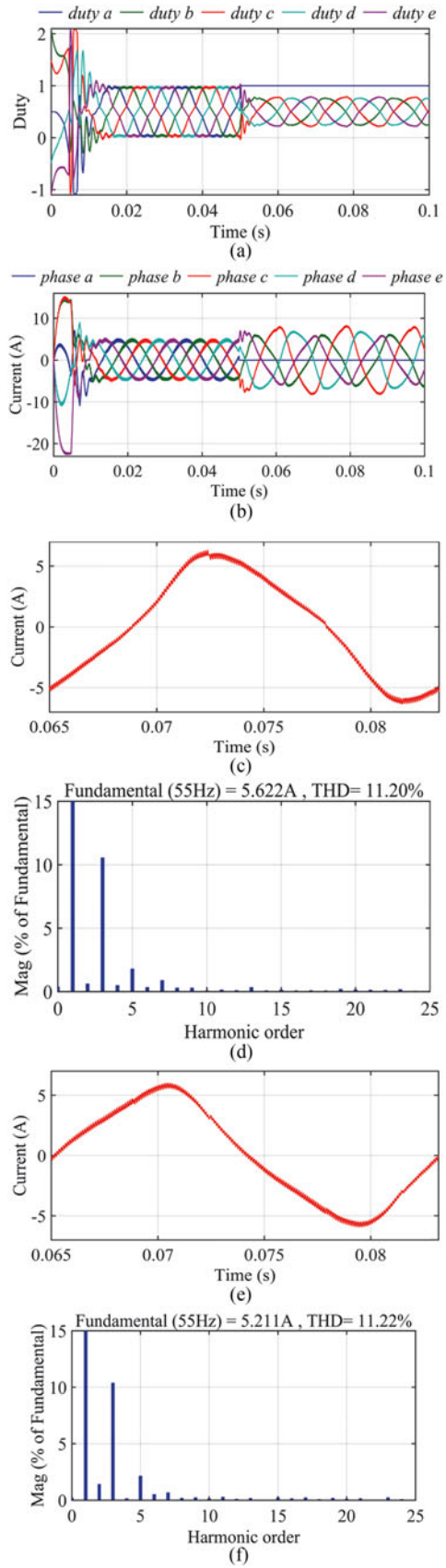

Fig. 13. Simulated asymmetric SVPWM waveforms. (a) Duty cycle. (b) Stator current. (c) Phase B current. (d) Harmonic of phase B current. (e) Phase E current. (f) Harmonic of phase E current.

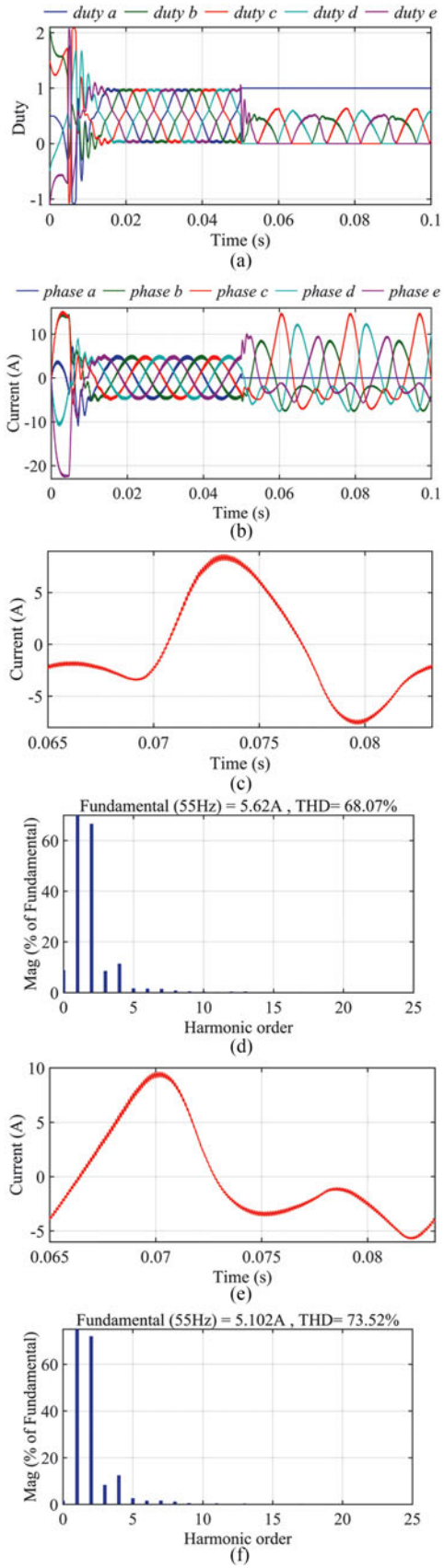

Fig. 14. Simulated symmetric SVPWM waveforms. (a) Duty cycle. (b) Stator current. (c) Phase B current. (d) Harmonic of phase B current. (e) Phase E current. (f) Harmonic of phase E current.

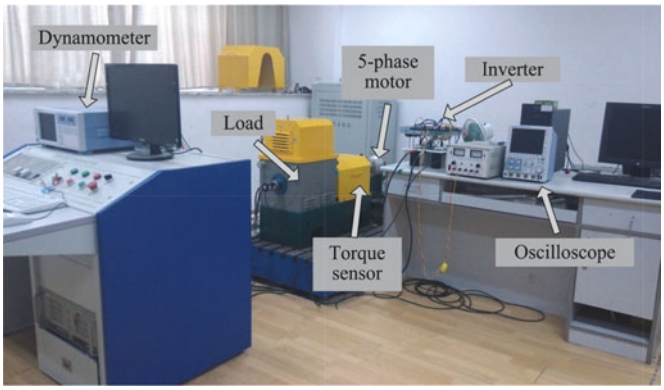

Fig. 15. Experimental platform.

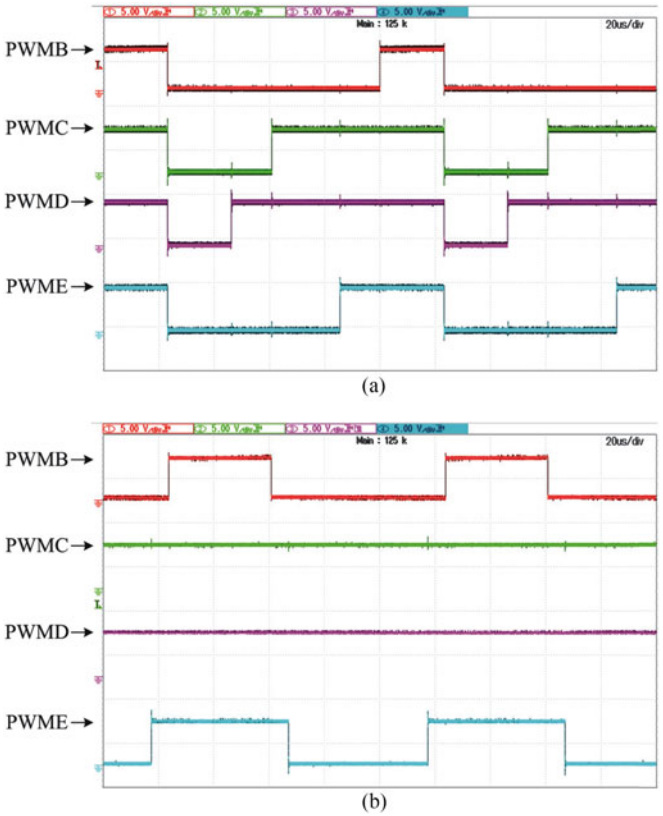

Fig. 16. PWM signals in sector 1 for two SVPWM methods. (a) Asymmetric SVPWM method. (b) Symmetric SVPWM method. (5 V/div, 0.02 ms/div)

Similarly, each switching device operates one time during a pried by the asymmetric SVPWM method. Thus, the high- and low-side switching devices bear nearly the same current amplitude and result in a smooth current. Moreover, since the whole system operates in the linear modulation range, the continuous SVPWM has lower harmonic component than the discontinuous SVPWM [28]. Therefore, the symmetric SVPWM has higher harmonic distortion rate than the asymmetric SVPWM, and the currents of the asymmetric SVPWM are smoother than those of the symmetric SVPWM.

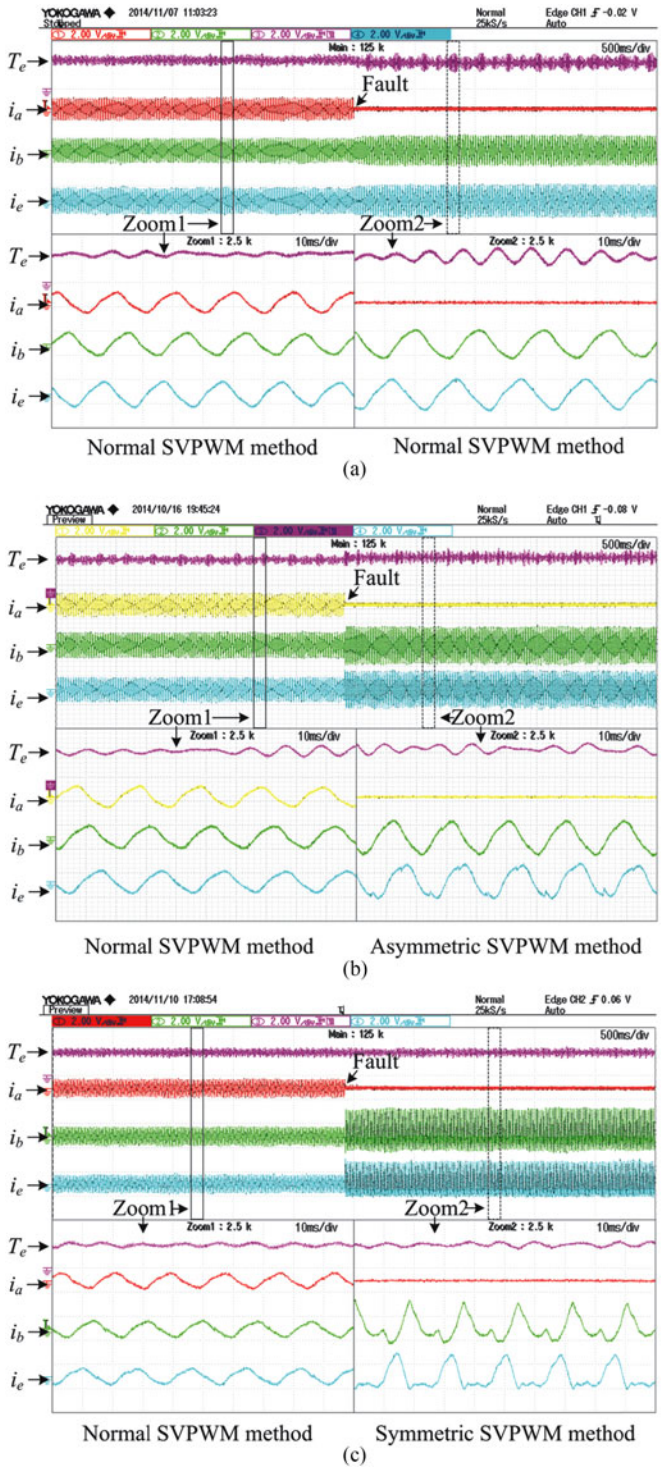

Fig. 17. Torque and currents under different conditions. (a) Normal SVPWM method. (b) Asymmetric SVPWM method. (c) Symmetric SVPWM method. (4 Nm/div, 20 A/div, 500 ms/div, 10 ms/div)

IV. Experimental Comparison

In order to further confirm the theoretical and simulation results, an experimental evaluation has been conducted. In Fig. 15, the digital signal processor is TI TMS320F2812, the intelligent

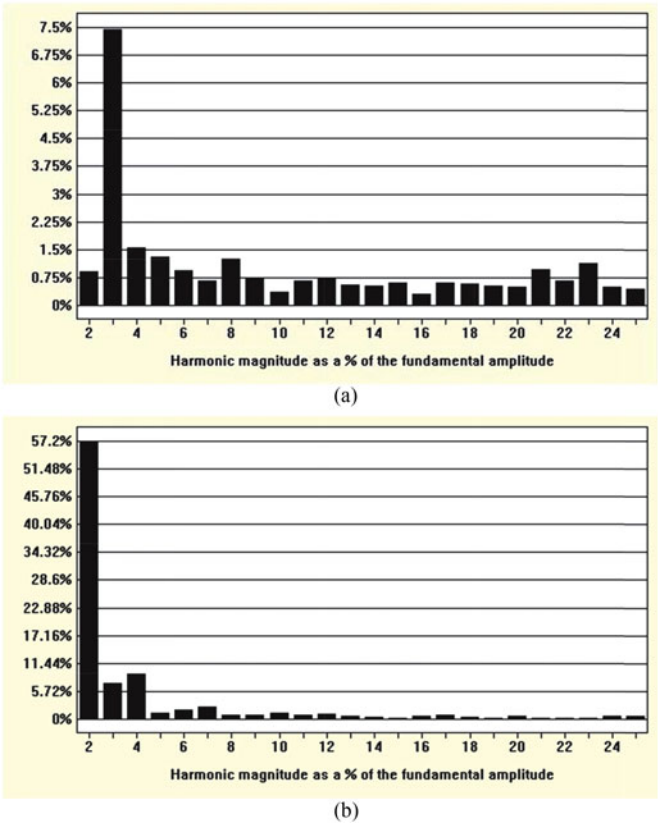

Fig. 18. Harmonic of phase B current by two SVPWM methods. (a) Asymmetric SVPWM method. (b) Symmetric SVPWM method.

TABLE III
EFFICIENCY OF DIFFERENT SVPWM METHODS

SVPWM	Normal SVPWM	Asymmetric SVPWM	Symmetric SVPWM
Efficiency	86.71%	81.37%	79.45%

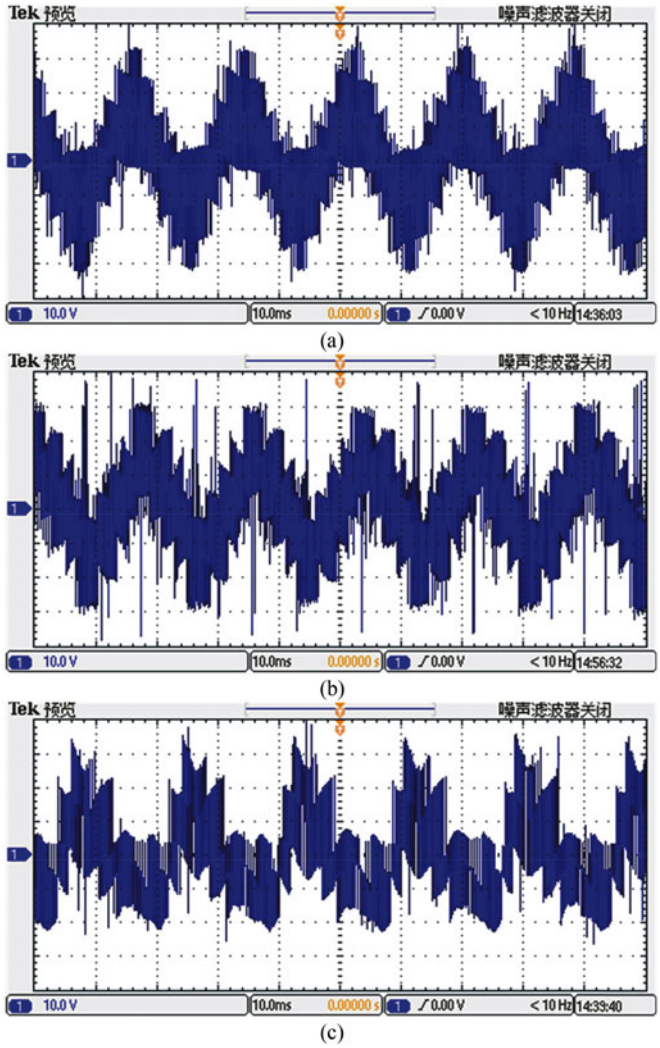

Fig. 19. Line voltage under health and fault situations. (a) Normal SVPWM method. (b) Asymmetric SVPWM method. (c) Symmetric SVPWM method (10 A/div, 10 ms/div).

power module is PM100CVA120, the torque sensor is HBM T20WN, the oscilloscope is YOKOGAMA DLM2054, and the current sensor is Tek A622 current clamp. Moreover, a dc motor is used as a load of the five-phase PM motor.

Fig. 16 gives the PWM signals from phase B to phase E in sector 1. Since the intelligent powermodule is low-level active, the real PWM signals are opposite of Figs. 7 and 9. Since the switching signals of phase A are set to high level, the switch transistors of the leg are OFF. So, the duty of phase A is 0. It is obvious that the asymmetric SVPWM is edge-aligned and $\mathrm{Duty}\_d > \mathrm{Duty}\_c > \mathrm{Duty}\_e > \mathrm{Duty}\_b$, while the symmetric SVPWM are center aligned and $\mathrm{Duty}\_c = \mathrm{Duty}\_d > \mathrm{Duty}\_e > \mathrm{Duty}\_b$.

Fig. 17 shows the torque and current waveforms by three SVPWM methods. The sequence of these waveforms is torque, phase A current, phase B current, and phase E current (from top to bottom). Fig. 17(a) shows the performances under health and fault condition by normal SVPWM method. Zoom1 and Zoom2 are the health and the fault ones, respectively. After the fault occurs, the torque ripple and the current amplitude increase at a certain extent. Fig. 17(b) and (c) exhibit the health and faulty performances by proposed strategies. Although the current amplitude still increase, the torque ripple is effectively reduced.

Fig. 18 compares the harmonic order of phase B current by two SVPWM methods. Fig. 18(a) is by the asymmetric SVPWM method and Fig. 18(b) is by the symmetric SVPWM method. The major harmonic of the asymmetric method is the third harmonic, while the symmetric SVPWM method is the second order. Moreover, the harmonic magnitude of the symmetric SVPWM method is much higher than that of the asymmetric SVPWM method.

The drive system efficiency by different SVPWM methods are shown in Table III. The efficiency is obtained from the following function:

$$\eta = P_{\mathrm{out}}/P_{\mathrm{in}} \tag{17}$$

where $P_{\rm out}$ is the output power and $P_{\rm in}$ is the input power. The power is obtained by the motor dynamometer. When the open-circuit fault occurs, the efficiency of the drive system decreases. The asymmetric SVPWM has lower efficiency than the symmetric SVPWM. Since the currents by the symmetric SVPWM have more harmonic than the asymmetric SVPWM, the efficiency of the asymmetric SVPWM method is higher than the symmetric SVPWM.

Fig. 19 displays the line voltage under normal and fault conditions. Fig. 19(a) is the voltage under normal operation. Fig. 19(b) and (c) show the waveforms under fault situation by two fault-tolerant SVPWM methods. It can be seen that these experimental results have a good agreement with the theoretical analysis and the simulated results. By comparing the experimental results of two strategies, it can be concluded that the asymmetric SVPWM has lesser harmonic component and more symmetric waveforms than the symmetric one. The symmetric SVPWM, which has higher positive current and relatively lower negative current, may cause damage to inverters.

V. Conclusion

In this paper, two fault-tolerant SVPWM strategies for a five-phase PM motor have been newly proposed during the loss of one phase. A frame reference based on hysteresis control has been applied to construct the new active space voltage vectors. Two different vector selection methods have been presented to form two fault-tolerant SVPWM strategies. This study has realized a fully SVPWM control on not only health condition, but also open-phase fault situation. The torque, line voltage, current, and its harmonic have been analyzed in simulations and experiments. Although both methods can track the reference speed and has almost the same torque ripple when fault occurs, the asymmetric SVPWM method has much smoother current, lower harmonic component and smaller damage to inverters than the symmetric SVPWM scheme.

References

[1] E. Levi, "Multiphase electric machines for variable-speed applications," *IEEE Trans. Ind. Electron.*, vol. 55, no. 5, pp. 1893–1909, May 2008.

[2] W. Zhao, M. Cheng, W. Hua, H. Jia, and R. Cao, "Back-EMF harmonic analysis and fault-tolerant control of flux-switching permanent-magnet machine with redundancy," *IEEE Trans. Ind. Electron.*, vol. 58, no. 5, pp. 1926–1936, May 2011.

[3] D. Glose and R. Kennel, "Carrier-based pulse width modulation for symmetrical six-phase drives," *IEEE Trans. Power Electron.*, vol. 30, no. 12, pp. 6873–6882, Dec. 2015.

[4] Q. Chen, G. Liu, W. Gong, and W. Zhao, "A new fault-tolerant permanent-magnet motor for electric vehicle applications," *IEEE Trans. Magn.*, vol. 47, no. 10, pp. 4183–4186, Oct. 2011.

[5] R. Cao, C. Mi, and M. Cheng, "Quantitative comparison of flux-switching permanent-magnet motors with interior permanent magnet motor for EV, HEV, and PHEV applications," *IEEE Trans. Magn.*, vol. 48, no. 8, pp. 2374–2384, Aug. 2012.

[6] I. Subotic, N. Bodo, and E. Levi, "An EV drive-train with integrated fast charging capability," *IEEE Trans. Power Electron.*, vol. 31, no. 2, pp. 1461–1471, Feb. 2016.

[7] M. J. Duran, J. Prieto, and F. Barrero, "Space vector PWM with reduced common-mode voltage for five-phase induction motor drives operating in overmodulation zone," *IEEE Trans. Power Electron.*, vol. 28, no. 8, pp. 4030–4040, Jul. 2013.

[8] M. J. Duran, J. Prieto, F. Barrero, J. A. Riveros, and H. Guzman, "Space-vector PWM with reduced common-mode voltage for five-phase induction motor drives," *IEEE Trans. Ind. Electron.*, vol. 60, no. 10, pp. 4159–4168, Oct. 2013.

[9] O. Dordevic, E. Levi, and M. Jones, "A vector space decomposition based space vector PWM algorithm for a three-level seven-phase voltage source inverter," *IEEE Trans. Power Electron.*, vol. 28, no. 2, pp. 637–649, Feb. 2013.

[10] D. Dujic, M. Jones, E. Levi, J. Prieto, and F. Barrero, "Switching ripple characteristics of space vector PWM schemes for five-phase two-level voltage source inverters-part 1: flux harmonic distortion factors," *IEEE Trans. Ind. Electron.*, vol. 58, no. 7, pp. 2789–2798, Jul. 2011.

[11] M. Jones, D. Dujic, E. Levi, J. Prieto, and F. Barrero, "Switching ripple characteristics of space vector PWM schemes for five-phase two-level voltage source inverters-part 2: current ripple," *IEEE Trans. Ind. Electron.*, vol. 58, no. 7, pp. 2799–2808, Jul. 2011.

[12] H. S. Che, E. Levi, M. Jones, H. Ping, and N. Abd Rahim, "Current control methods for an asymmetrical six-phase induction motor drive," *IEEE Trans. Power Electron.*, vol. 29, no. 1, pp. 407–417, Jan. 2014.

[13] C. Zhou, G. Yang, and J. Su, "PWM strategy with minimum harmonic distortion for dual three-phase permanent-magnet synchronous motor drives operating in the overmodulation region," *IEEE Trans. Power Electron.* , vol. 31, no. 2, pp. 1367–1380, Mar. 2015.

[14] N. Bianchi, S. Bolognani, and M. Pre, "Strategies for the fault-tolerant current control of a five-phase permanent-magnet motor," *IEEE Trans. Ind. Appl.*, vol. 43, no. 3, pp. 960–970, Jul./Aug. 2007.

[15] W. Zhao, M. Cheng, K. T. Chau, J. Ji, and R. Cao, "Remedial injected harmonic current operation of redundant flux-switching permanent magnet motor drives," *IEEE Trans. Ind. Electron.*, vol. 60, no. 1, pp. 151–159, Jan. 2013.

[16] H. S. Che, M. J. Duran, E. Levi, M. Jones, H. Wooi-Ping, and N. Abd Rahim, "Postfault operation of an asymmetrical six-phase induction machine with single and two isolated neutral points," *IEEE Trans. Power Electron.*, vol. 29, no. 19, pp. 5406–5416, Oct. 2014.

[17] X. Jiang, W. Huang, R. Cao, Z. Hao, and W. Jiang, "Electric drive system of dual-winding fault-tolerant permanent magnet motor for aerospace applications," *IEEE Trans. Ind. Electron.*, vol. 62, no. 12, pp. 7322–7330, Dec. 2015.

[18] H. Guzman, M. J. Duran, F. Barrero, B. Bogado, and S. Toral, "Speed control of five-phase induction motors with integrated open-phase fault operation using model-based predictive current control techniques," *IEEE Trans. Ind. Electron.*, vol. 61, no. 9, pp. 4474–4484, Sep. 2014.

[19] S. Dwari and L. Parsa, "Fault-tolerant control of five-phase permanent-magnet motors with trapezoidal back EMF," *IEEE Trans. Ind. Electron.*, vol. 58, no. 2, pp. 476–485, Feb. 2011.

[20] A. Mohammdpour, S. Mishra, and L. Parsa, "Fault-tolerant operation of multiphase permanent-magnet motors using iterative learning control," *IEEE J. Emerg. Sel. Topics Power Electron.*, vol. 2, no. 2, pp. 201–211, Jun. 2014.

[21] M. Salehifar, R. S. Arashloo, J. M. Moreno-Equilaz, V. Sala, and L. Romeral, "Fault detection and fault tolerant operation of a five phase PM motor drive using adaptive model identification approach," *IEEE J. Emerg. Sel. Topics Power Electron.*, vol. 2, no. 2, pp. 212–223, Jun. 2014.

[22] A. Mohammadpour and L. Parsa, "A unified fault-tolerant current control approach for five-phase PM motors with trapezoidal Back EMF under different stator winding connections," *IEEE Trans. Power Electron.*, vol. 28, no. 7, pp. 3517–3527, Jul. 2013.

[23] M. Aboelhassan, T. Raminosoa, D. Goodman, L. D. Lillo, and C. Gerada, "Performance evaluation of a vector-control fault-tolerant flux-switching motor drive," *IEEE Trans. Ind. Electron.*, vol. 60, no. 8, pp. 2997–3006, Aug. 2013.

[24] F. J. Lin, Y. C. Hung, J.C. Hwang, and M. T. Tsai, "Fault-tolerant control of a six-phase motor drive system using a Takagi–Sugeno–Kang type fuzzy neural network with asymmetric membership function," *IEEE Trans. Power Electron.*, vol. 28, no. 7, pp. 3557–3572, Jul. 2013.

[25] A. Tani, M. Mengoni, L. Zarri, G. Serra, and D. Casadei, "Control of multiphase induction motors with an odd number of phases under open-circuit phase faults," *IEEE Trans. Power Electron.*, vol. 27, no. 2, pp. 565–577, Feb. 2012.

[26] A. Iqbal and S. Moinuddin, "Comprehensive relationship between carrier-based pwm and space vector PWM in a five-phase VSI," *IEEE Trans. Power Electron.*, vol. 24, no. 10, pp. 2379–2390, Oct. 2009.

[27] Q. Chen, G. Liu, W. Zhao, L. Sun, M. Shao, and Z. Liu, "Design and comparison of two fault-tolerant interior-permanent-magnet motors," *IEEE Trans. Ind. Electron.*, vol. 61, no. 12, pp. 6615–6623, Dec. 2014.

[28] S. An, X. Sun, Q. Zhang, Y. Zhong, and B. Ren, "Study on the novel generalized discontinuous SVPWM strategies for three-phase voltage source inverters," *IEEE Trans. Ind. Inf.*, vol. 9, no. 2, pp. 781–789, May 2013.

Guohai Liu (M'07–SM'15) received the B.Sc. degree from Jiangsu University, Zhenjiang, China, in 1985, and the M.Sc. and Ph.D. degrees from Southeast University, Nanjing, China, in 1988 and 2002, respectively, in electrical engineering and control engineering.

Since 1988, he has been with Jiangsu University, where he is currently a Professor, the Dean of the School of Electrical Information Engineering. His teaching and research interests include electrical machines, motor drives for electric vehicles, and intelligent control. He has authored or coauthored more than 150 technical papers and 4 textbooks, and holds 15 patents in these areas.

Li Qu received the B.Sc. and M.Sc. degrees in electrical engineering from Jiangsu University, Zhenjiang, China, in 2012 and 2015, respectively.

Her current research interests include control of permanent-magnet motors.

Wenxiang Zhao (M'08–SM'14) received the B.Sc. and M.Sc. degrees in electrical engineering from Jiangsu University, Zhenjiang, China, in 1999 and 2003, respectively, and the Ph.D. degree in electrical engineering from Southeast University, Nanjing, China, in 2010.

He has been with Jiangsu University since 2003, where he is currently a Professor with the School of Electrical Information Engineering. From 2008 to 2009, he was a Research Assistant with the Department of Electrical and Electronic Engineering, University of Hong Kong, Hong Kong. From 2013 to 2014, he was a Visiting Professor with the Department of Electronic and Electrical Engineering, University of Sheffield, Sheffield, U.K. His current research interests include electric machine design, modeling, fault analysis, and intelligent control. He has authored and coauthored more than 130 technical papers in these areas.

Qian Chen received the B.Sc. and Ph.D. degrees in electrical engineering from Jiangsu University, Zhenjiang, China, in 2009 and 2015, respectively.

His current research interests include design and control of electric machine.

Ying Xie received the B.Sc. and M.Sc. degrees in electrical engineering from Jiangsu University, Zhenjiang, China, in 2012 and 2015, respectively.

His current research interests include permanent-magnet motors and their drivers.